

Article

Open Access



Enhanced all-weather sodium-ion batteries performance in a low-defect and Na-enriched Prussian blue analogue cathode by nickel substitution

Jingwen Zhang¹, Jing Wan², Mingyang Ou¹, Siying Liu¹, Bicheng Huang¹, Jia Xu¹, Shixiong Sun¹, Yue Xu¹, Yaqing Lin^{1*}, Chun Fang^{1*}, Jiantao Han¹

¹State Key Laboratory of Material Processing and Die & Mould Technology, School of Materials Science and Engineering, Huazhong University of Science and Technology, Wuhan 430074, Hubei, China.

²Department of Applied Physics, Chongqing University, Chongqing 401331, China.

* **Correspondence to:** Yaqing Lin, State Key Laboratory of Material Processing and Die & Mould Technology, School of Materials Science and Engineering, Huazhong University of Science and Technology, Wuhan 430074, Hubei, China. E-mail: 359702366@qq.com; Dr. Assoc. Prof. Chun Fang, a State Key Laboratory of Material Processing and Die & Mould Technology, School of Materials Science and Engineering, Huazhong University of Science and Technology, Wuhan 430074, Hubei, China. E-mail: fangchun@hust.edu.cn

How to cite this article: Zhang J, Wan J, Ou M, Liu S, Huang B, Xu J, Sun S, Xu Y, Lin Y, Fang C, Han J. Enhanced all-weather sodium-ion batteries performance in a low-defect and Na-enriched Prussian blue analogue cathode by nickel substitution. *Energy Mater* 2023;3:300008. <https://dx.doi.org/10.20517/energymater.2022.71>

Received: 31 Oct 2022 **First Decision:** 5 Dec 2022 **Revised:** 26 Dec 2022 **Accepted:** 19 Jan 2023 **Published:** 14 Feb 2023

Academic Editors: Yuping Wu, Jiazhao Wang **Copy Editor:** Fangling Lan **Production Editor:** Fangling Lan

Abstract

Cobalt hexacyanoferrate (CoHCF) is one of the most promising cathode materials for all-weather sodium-ion batteries (SIBs) due to its open three-dimensional (3D) framework structures, high theoretical specific capacity, good voltage platform and almost no Jahn-Teller effects. However, CoHCF still suffers from poor cycling stability and bad rate capability, which is closely related to the huge distortion of frame structure and poor conductivity. In this study, by choosing nickel (Ni) to partially replace cobalt (Co) in the CoHCF lattice, we successfully prepared low-defect and Na-enriched $\text{Na}_2\text{Co}_{0.7}\text{Ni}_{0.3}[\text{Fe}(\text{CN})_6]$ ($\text{Co}_{0.7}\text{Ni}_{0.3}\text{HCF}$) in chelate and sodium salt-assisted coprecipitation method. Both experiments and first-principles calculations demonstrate that Ni substitution can effectively suppress the lattice distortion during the charging and discharging process of CoHCF. Furthermore, the introduction of Ni increases ion mobility by reducing the ion migration barrier (0.31 eV versus 0.17 eV) and improves the electronic conductivity by reducing the bandgap. It is found that $\text{Co}_{0.7}\text{Ni}_{0.3}\text{HCF}$ exhibits superior electrochemical performance compared with that of CoHCF in a wide temperature range (-30 to 60 °C). At 25 °C,



© The Author(s) 2023. **Open Access** This article is licensed under a Creative Commons Attribution 4.0 International License (<https://creativecommons.org/licenses/by/4.0/>), which permits unrestricted use, sharing, adaptation, distribution and reproduction in any medium or format, for any purpose, even commercially, as long as you give appropriate credit to the original author(s) and the source, provide a link to the Creative Commons license, and indicate if changes were made.



$\text{Co}_{0.7}\text{Ni}_{0.3}\text{HCF}$ delivers a high specific capacity of 142.2 mAh g^{-1} at 0.2 C , an ultrahigh rate capability with 126.2 mAh g^{-1} at 5 C and excellent cycling stability with 80.9% capacity retention after 500 cycles at 5 C . Even at $-30 \text{ }^\circ\text{C}$, $\text{Co}_{0.7}\text{Ni}_{0.3}\text{HCF}$ can provide a high capacity of 109 mAh g^{-1} without an activation process. This work reveals the great application prospect of PBAs for all-climate SIBs, especially at low temperatures.

Keywords: Prussian blue analogues, all-climate, sodium-ion batteries, CoHCF, Ni substitution

INTRODUCTION

The application of Lithium-ion batteries (LIBs) in the field of energy storage, especially at low temperatures, has been limited due to the shortage of lithium resources, high raw material prices, and unsatisfactory low-temperature performances. Having similar physical and chemical properties to lithium, low-cost sodium-ion batteries (SIBs) are one of the potential options for large-scale energy storage^[1-3]. Meanwhile, the Stokes radius of sodium-ion is smaller than that of lithium-ion, which is more conducive to kinetic transmission and has better performance at subzero temperatures^[4,5]. In addition, in the cathode materials of SIBs, Prussian blue (PB) and its analogues (PBAs, $\text{Na}_2\text{M}[\text{Fe}(\text{CN})_6]$, $\text{M} = \text{Fe, Co, Mn, Ni, Cu, etc.}$) have an open 3D framework structure, which can further improve the migration rate of Na^+ -ions^[6-8]. However, the PBAs synthesized via the conventional rapid precipitation process are always Na^+ -deficient phase with large amounts of water and $\text{Fe}(\text{CN})_6^{4-}$ vacancies, which leads to low capacity and poor cycling and rate stability^[9-11]. The use of chelates including sodium citrate^[12], ethylenediaminetetraacetic acid (EDTA)^[13], sodium carboxymethylcellulose (CMC)^[14] and additives such as surfactants^[15] and sodium salts^[16] has improved the control of crystallization, which are propitious to increase sodium content and reduce defects of PBAs.

Among the PBAs, nickel hexacyanoferrate (NiHCF) has only one redox center, severely limiting the capacity, iron hexacyanoferrate (FeHCF) with low average voltage will also reduce the energy density, and manganese hexacyanoferrate (MnHCF) is affected by Jahn-Teller effect, resulting in poor cycling performance. Whereas, CoHCF shows attractive advantages such as high theoretical capacity, good voltage platform and almost no Jahn-Teller effects^[17-19]. However, even in the PB with perfect lattice, once the material reaches its theoretical specific capacity (fully desodiated state), the material will undergo huge volume change after almost all sodium ions are removed from the framework, resulting in stress and strain. The accumulation of stress and strain causes large lattice distortion and even collapse of the lattice structure, resulting in poor cycling stability^[20]. Therefore, many strategies have been proposed to stabilize the lattice structures, including surface protective layers coating^[21-23], transition metal elements doping^[24-26], and regulation of lattice water^[27,28]. Qiao *et al.* constructed a semiconductor ZnO protective layer outside FeHCF to form a physical barrier, which inhibited the decomposition of PB during the charging and discharging process and improved the electrochemical performance^[23]. Wang *et al.* achieved Ni gradient doping from surface to inside of FeHCF, in which the nickel-rich outer layer provided a stable framework structure and the nickel-poor inner layer partly activated the electrochemical activity of Fe to increase the capacity^[25]. Hu *et al.* used interstitial water as the pillar in the crystal frameworks to stabilize the lattice, which effectively improved the cycling stability of PBAs^[27]. However, the lattice water occupies the Na^+ sites, which directly reduces the sodium content in the lattice and results in the decrease of specific capacity^[29,30]. Therefore, it is a great challenge to choose appropriate modification methods to balance high capacity and cycle stability. Meanwhile, only under a stable frame structure, sodium ions can fully use the advantages of 3D channels in PBAs, exhibiting good rate and low-temperature performances, and be applied to all-climate batteries.

In this study, to balance the high specific capacity and good cycle stability of PBAs, in the synthesis strategy of $\text{Co}_{0.7}\text{Ni}_{0.3}\text{HCF}$, we used chelate and sodium salt-assisted coprecipitation crystallization method to obtain the low-defect and Na-enriched PBA to ensure its high specific capacity. Moreover, we chose Ni to replace Co partially to further stabilize the lattice structure, improving the cycling stability. The results of inductively coupled plasma-optical emission spectrometer (ICP-OES) and thermogravimetric analysis (TGA) indicate that $\text{Co}_{0.7}\text{Ni}_{0.3}\text{HCF}$ has a Na-enriched and low-defect structure. *Ex-situ* X-ray diffraction (XRD) reveals that $\text{Co}_{0.7}\text{Ni}_{0.3}\text{HCF}$ has smaller volume change and better phase transition reversibility during charging and discharging process than CoHCF. Furthermore, the first-principles calculations show that the Ni substitution of CoHCF can improve the conductivity and reduce the sodium-ion migration barrier. Galvanostatic intermittent titration technique (GITT) tests also exhibit that $\text{Co}_{0.7}\text{Ni}_{0.3}\text{HCF}$ has a higher Na^+ diffusion coefficient. Both of them explain why the synthesized $\text{Co}_{0.7}\text{Ni}_{0.3}\text{HCF}$ has good electrochemical performance at low temperatures and high rates. $\text{Co}_{0.7}\text{Ni}_{0.3}\text{HCF}$ shows excellent electrochemical performance in a wide temperature range (-30 to 60 °C). It exhibits an ultrahigh specific capacity (142.2 mAh g^{-1} at 0.2 C), high rate capability (126.2 mAh g^{-1} at 5 C) and excellent cycling stability with 80.9% capacity retention after 500 cycles at 5 C at room temperature. At -30 °C, $\text{Co}_{0.7}\text{Ni}_{0.3}\text{HCF}$ can still provide 109 mAh g^{-1} without an activation process. In addition, $\text{Co}_{0.7}\text{Ni}_{0.3}\text{HCF}$ also shows stable electrochemical performance at higher temperatures of 45 °C and 60 °C due to a stable framework. This work confirms that the low-defect and Na-enriched synthesis methods have obtained CoHCF with low structural defects, and the introduction of Ni further improves the structural stability. Also, Ni substitution improves the conductivity and diffusion kinetics of the materials, making $\text{Co}_{0.7}\text{Ni}_{0.3}\text{HCF}$ a powerful candidate for the cathode of all-weather high-energy sodium-ion batteries.

EXPERIMENTAL

Materials synthesis

A series of $\text{Na}_2\text{Co}_x\text{Ni}_{1-x}[\text{Fe}(\text{CN})_6] \cdot y\text{H}_2\text{O}$ ($\text{Co}_x\text{Ni}_{1-x}\text{HCF}$) ($x = 0, 0.1, \dots, 1.0$) PBAs were synthesized by coprecipitation method. Solution A was formed by dissolving $2x$ mmol $\text{CoCl}_2 \cdot 6\text{H}_2\text{O}$, $2(1-x)$ mmol $\text{NiCl}_2 \cdot 6\text{H}_2\text{O}$, 10 mmol trisodium citrate and 4 g NaCl in 50 mL DI water. Solution B was formed by dissolving 2 mmol $\text{Na}_4\text{Fe}(\text{CN})_6 \cdot 10\text{H}_2\text{O}$ in 50 mL DI water. Then, solution A was dropped into solution B simultaneously by a peristaltic pump with magnetic stirring for 4 h and aged for 24 h at 30 °C. The precipitated products were collected by centrifugation and washed thoroughly with deionized water and ethanol several times. Finally, after drying at 105 °C in a vacuum oven for 24 h, samples were collected and named $\text{Co}_x\text{Ni}_{1-x}\text{HCF}$ ($x = 0, 0.1, \dots, 1.0$). CoHCF and $\text{Co}_{0.7}\text{Ni}_{0.3}\text{HCF}$ were synthesized as described process above when $x = 1$ and $x = 0.7$, respectively.

Materials characterization

XRD measurement was performed by Cu $K\alpha$ radiation ($\lambda = 1.541874 \text{ \AA}$) in a scan range (2θ) of 10–80° on Panalytical X'pert PRO MRD. The scanning electron microscope (SEM, Japan) was used to collect FESEM images to display the morphology of the samples at an acceleration voltage of 30 kV. The transmission electron microscopy (TEM, Tecnai G2 F30 S-TWIN, FEI) was used to obtain TEM images of the cathode. The thermogravimetry measurements were performed using a NETZSCH-STA449c/3/G analyzer from 30 to 500 °C at a heating rate of 10 °C/min in N_2 . The Fourier transform infrared (FTIR) spectra were obtained by A VERTEX 70 FT-IR spectrometer (4000–500 cm^{-1} region). The composition of PBAs was measured by ICP-OES (IRIS Intrepid IIXSP, Thermo Elemental, USA). X-ray photoelectron spectroscopy (XPS) analysis was conducted through a Thermo ESCALAB 250XI instrument.

Electrochemical measurement

For the electrochemical performance tests of PBAs, CR2025 coin cells were assembled in a glove box filled with pure Ar gas. The working electrodes were made by painting the uniform slurry which contained the

active material (70%), Ketjen black (conductive agent, 10%), Super P (conductive agent, 10%), sodium carboxymethylcellulose (NaCMC, binder, 5%) and styrene butadiene rubber (SBR, binder, 5%)^[31,32] onto an aluminum foil and then drying in a vacuum oven at 105 °C for 12 h. The mass loading of active materials was about 1.5–3 mg cm⁻¹ for the electrodes. The metallic sodium anode is used as the counter electrode. The composition of the electrolyte was 1 mol L⁻¹ NaClO₄ in ethylene carbonate (EC)/ propylene carbonate (PC) (1:1 v/v) with 2% fluoroethylene carbonate (FEC) as an additive (by volume). The separator was glass fibers (GF/D) from Whatman. Cyclic voltammetry (CV) was conducted on an electrochemical workstation (CHI760E) between 2.0 and 4.2 V versus Na⁺/Na at a scan rate of 0.1 mV s⁻¹. Galvanostatic intermittent titration technique (GITT) testing of the charging and discharging process was performed on a Land battery system at a current density of 15 mA g⁻¹ from 2.0–4.2 V, in which the coin cell was alternately charged for 10 min, followed by an interval of 60 min.

Calculation method

The first-principles calculations were performed within the density functional theory framework by using the projector augmented wave (PAW) method, as implemented in the Vienna ab initio simulation package (VASP)^[33,34]. The generalized gradient approximation (GGA) with Perdew-Burke-Ernzerhof (PBE) was used to treat the exchange-correlation interactions^[35]. The energy and force convergence values were chosen as 10⁻⁵ eV and 0.01 eV Å⁻¹, respectively. The Kohn-Sham orbitals were expanded in plane waves with a kinetic energy cut-off of 500 eV. The Brillouin zone integration and *k*-point sampling were performed with a Monkhorst-Pack scheme of 3 × 3 × 3 grid for all calculations^[36]. The GGA + *U* correlation method was used and the *U* value of Fe, Co and Ni atoms were set as 4, 3.4 and 6 eV, respectively^[37]. The diffusion barrier energies of sodium ions were explored using the climbing image nudged elastic band (CI-NEB) method^[38].

RESULTS AND DISCUSSION

Structure analysis

XRD patterns of a series of Co_xNi_{1-x}[Fe(CN)₆] PBAs with different ratios of Co and Ni (*x* = 0, 0.1, ..., 1.0) show monoclinic phase with a space group of P21/n [Supplementary Figure 1A], suggesting high Na content of series of samples^[15,39]. The refined results for Co_{0.7}Ni_{0.3}HCF [Figure 1A] and CoHCF [Supplementary Figure 1B] were from Fullprof software^[40-45], and it demonstrates the lattice parameters of Co_{0.7}Ni_{0.3}HCF with *a* = 10.3656(5) Å, *b* = 7.4286(4) Å, *c* = 7.2269(4) Å, $\alpha = \gamma = 90^\circ$, $\beta = 92.805(3)^\circ$. About CoHCF, *a* = 10.4118(7) Å, *b* = 7.4573(5) Å, *c* = 7.2608(5) Å, $\alpha = \gamma = 90^\circ$, $\beta = 92.730(4)^\circ$, as shown in Supplementary Table 1. The crystal structure of Co_{0.7}Ni_{0.3}HCF [Figure 1B] indicates the ∠Fe-C-N and ∠C-N-Co (Ni) bond angles are deflected from the typical 180° because of the large accommodation of Na⁺. In the PBAs lattice, different types of water are removed at different temperatures. The water of Prussian blue analogues (PBAs) can be divided into adsorbed water, interstitial water and coordinated water, which occupy the surface, lattice gap and Fe(CN)₆⁴⁻ vacancy of PBAs, respectively. Because the adsorbed water is on the surface of the materials, it can be removed by simple heating and drying. The interstitial water can be forcibly removed by increasing the heating temperature. Removal of coordinated water is even more difficult and this may also lead to the destruction of the material structure^[27]. The occupancy of R $\bar{3}m$ in the cubic lattice of PBAs was detected by neutron diffraction and extended X-ray absorption fine structure (EXAFS). The lattice water can occupy sites of 8 c, 32 f and 48 g^[30]. It is not difficult to find that the occupied sites of water molecules coincide with the occupied sites of sodium ions. As shown in the TGA curves [Figure 1C], the content of water of Co_{0.7}Ni_{0.3}HCF and CoHCF is very low due to very small amounts of vacancies formed inside the crystal structure during the effectively controlled coprecipitation process. From room temperature to 105 °C, the weight loss of Co_{0.7}Ni_{0.3}HCF and CoHCF is about 0.4% and 0.7%, respectively, which can be ascribed to the loss of the adsorbed water on the surface. From 150 °C to 250 °C, the weight loss of interstitial water in the open frameworks of Co_{0.7}Ni_{0.3}HCF and CoHCF is 10.3% and 10.4%,

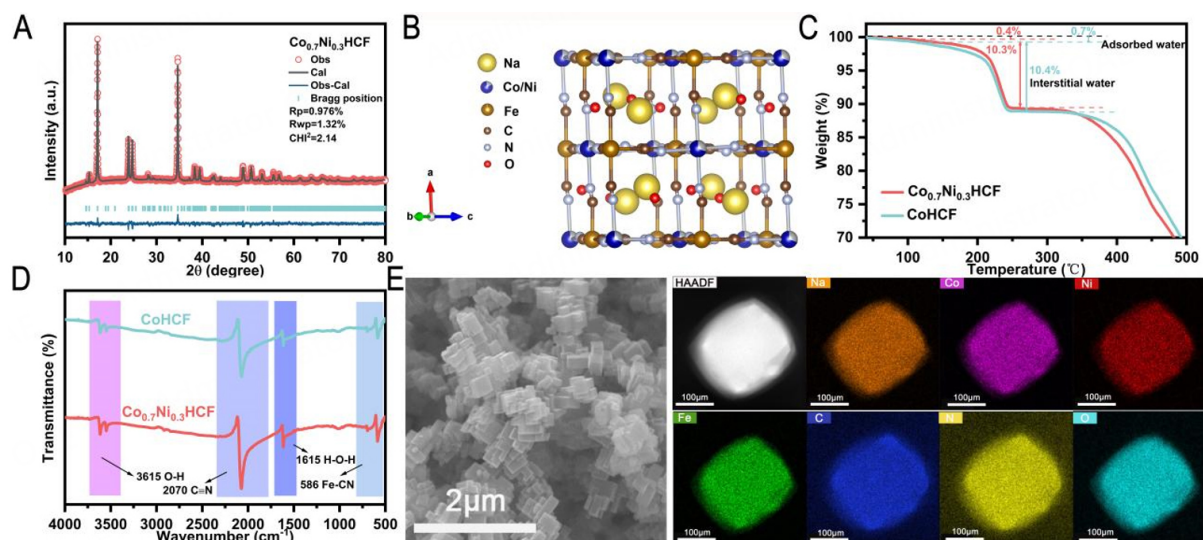


Figure 1. Analysis of the structure and morphology of the PBA samples. (A and B) Rietveld refinements and schematic illustrations of the structures of the $\text{Co}_{0.7}\text{Ni}_{0.3}\text{HCF}$. (C) TGA curves and (D) FTIR spectra of $\text{Co}_{0.7}\text{Ni}_{0.3}\text{HCF}$ and CoHCF . (E) SEM and Energy dispersive spectroscopy (EDS) images mapping of $\text{Co}_{0.7}\text{Ni}_{0.3}\text{HCF}$.

respectively. Combined with ICP-OES and TGA, the chemical compositions of two PBAs can be determined as $\text{Na}_{2.008}\text{Ni}_{0.269}\text{Co}_{0.731}[\text{Fe}(\text{CN})_6]_{0.997} \cdot 2.09\text{H}_2\text{O}$ and $\text{Na}_{2.047}\text{Co}[\text{Fe}(\text{CN})_6]_{0.997} \cdot 2.19\text{H}_2\text{O}$, respectively. It demonstrates the two PBAs samples show similar high Na and low vacancy contents. According to FTIR spectra [Figure 1D], the peaks at $\sim 3615\text{ cm}^{-1}$ and 1615 cm^{-1} are attributed to the O-H and H-O-H bending modes of the water molecules, the absorption peaks at $\sim 2070\text{ cm}^{-1}$ and 586 cm^{-1} are assigned to the stretching vibration of $\text{C}\equiv\text{N}$ and Fe-CN bonds, showing the characteristic functional groups of PBAs^[28]. The SEM images of $\text{Co}_{0.7}\text{Ni}_{0.3}\text{HCF}$ [Figure 1E] exhibit cubic morphologies with diameters ranging from 100 to 400 nm, which have sharp edges and corners. From the EDS images mapping, all elements of $\text{Co}_{0.7}\text{Ni}_{0.3}\text{HCF}$ are uniformly distributed throughout the particles.

Electrochemical performance at various temperatures

Figure 2A-E compares the electrochemical performance of $\text{Co}_{0.7}\text{Ni}_{0.3}\text{HCF}$ and CoHCF at $25\text{ }^\circ\text{C}$. In the electrochemical window of 2.0-4.2 V, nickel is generally considered inactive and unable to provide capacity in PBAs^[46]. Actually, the charge/discharge curves of $\text{Co}_x\text{Ni}_{1-x}\text{HCF}$ [Supplementary Figure 2A and B] clearly demonstrate that the specific capacities gradually decrease with the increasing content of Ni in $\text{Co}_x\text{Ni}_{1-x}\text{HCF}$ ($x = 1.0, 0.9, \dots, 0$), while the cycling stability is improved remarkably, as shown in Supplementary Figure 2C. Among different Ni-substituted electrodes, the $\text{Co}_{0.7}\text{Ni}_{0.3}\text{HCF}$ electrode shows the most excellent performance and is chosen for further investigations.

The cyclic voltammetry (CV) curve [Figure 2A] of CoHCF displays two pairs of well-defined and symmetric oxidation/redox peaks at 3.425 V/3.201 V and 3.886 V/3.743 V, corresponding to the redox reactions of N-coordinated $\text{Co}^{2+}/\text{Co}^{3+}$ and C-coordinated $\text{Fe}^{2+}/\text{Fe}^{3+}$ during the reversible sodium-ion insertion/extraction process respectively^[47], which agrees with the two charge/discharge voltage plateaus. $\text{Co}_{0.7}\text{Ni}_{0.3}\text{HCF}$ displays two pairs of oxidation/redox peaks at 3.428 V/3.218 V and 3.877 V/3.752 V, showing smaller voltage hysteresis of 0.210 V than CoHCF of 0.224 V. As shown in the Figure 2B and C, with the increasing of cycle numbers, the higher voltage plateau of CoHCF gradually vanishes, suggesting a decrease in the capacity contribution from the C-coordinated $\text{Fe}^{2+}/\text{Fe}^{3+}$ couple. Whereas for the $\text{Co}_{0.7}\text{Ni}_{0.3}\text{HCF}$, there is no obvious change in the charge/discharge profiles within the first 100 cycles, which exhibits much higher

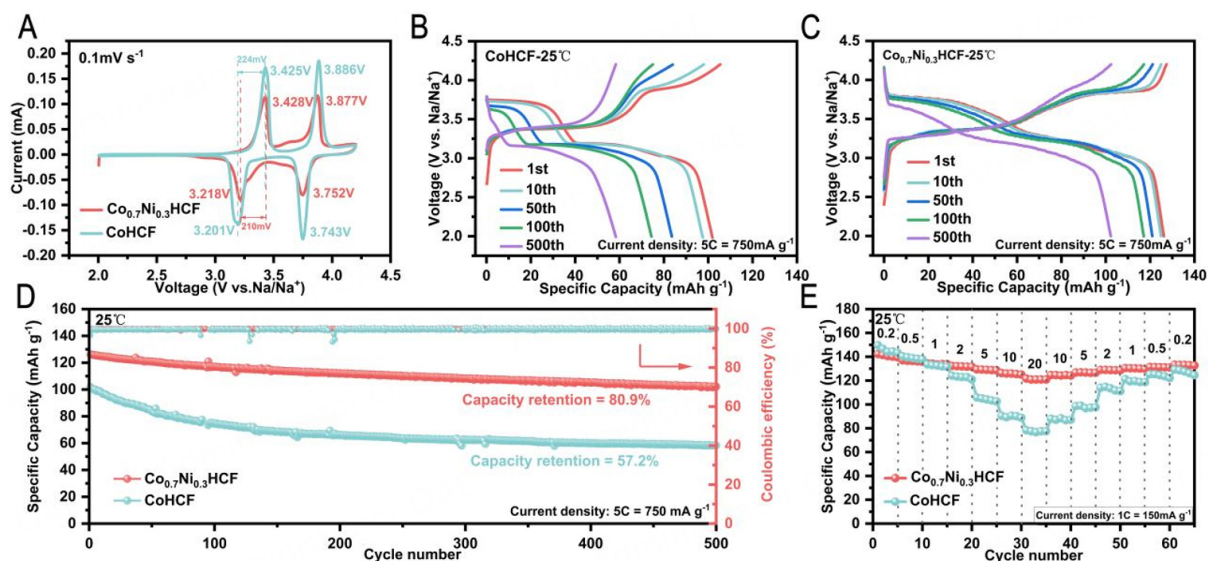


Figure 2. Electrochemical properties of $\text{Co}_{0.7}\text{Ni}_{0.3}\text{HCF}$ and CoHCF at 25 °C (1 C = 150 mA g^{-1}). (A) Typical CV curves measured at a scan rate of 0.1 mV s^{-1} . Charge/discharge voltage profiles of (B) $\text{Co}_{0.7}\text{Ni}_{0.3}\text{HCF}$ and (C) CoHCF at 5 C at different cycles. (D) Long-cycle performance at 5 C. (E) Rate performance at 0.2–20 C.

capacity retention of $\text{Co}_{0.7}\text{Ni}_{0.3}\text{HCF}$. It demonstrates the introduction of Ni can retain the redox activity of N-coordinated $\text{Co}^{2+}/\text{Co}^{3+}$ and C-coordinated $\text{Fe}^{2+}/\text{Fe}^{3+}$ for long cycles.

Figure 2D compares the capacity retention of $\text{Co}_{0.7}\text{Ni}_{0.3}\text{HCF}$ and CoHCF at 5 C. $\text{Co}_{0.7}\text{Ni}_{0.3}\text{HCF}$ delivers a specific discharge capacity of 126.2 mAh g^{-1} and a high capacity retention of 80.9% at 5 C after 500 cycles at 25 °C. In contrast, CoHCF only delivers a discharge capacity of 102.2 mAh g^{-1} and a lower capacity retention of 57.2% under similar charge and discharge conditions. Moreover, $\text{Co}_{0.7}\text{Ni}_{0.3}\text{HCF}$ displays an outstanding rate (0.2–20 C) capability, which is much superior to that of the CoHCF [**Figure 2E**]. In particular, $\text{Co}_{0.7}\text{Ni}_{0.3}\text{HCF}$ could deliver 142.2, 137.0, 134.4, 132.3, 129.4, 126.3 and 121.7 mAh g^{-1} at the rates of 0.2, 0.5, 1, 2, 5, 10 and 20 C, respectively, while the CoHCF delivers 149.7 mAh g^{-1} at 0.2 C but only retains a capacity of 78.4 mAh g^{-1} at 20 C. Charge/discharge voltage profiles of $\text{Co}_{0.7}\text{Ni}_{0.3}\text{HCF}$ and CoHCF at different rates are shown in **Supplementary Figure 3**. It is worth noting that $\text{Co}_{0.7}\text{Ni}_{0.3}\text{HCF}$ is the most competitive for rate performance among many reported PBAs cathode materials in SIBs, as shown in **Supplementary Figure 4A**. In addition, when the current density returns to 0.2 C, the discharge specific capacity of $\text{Co}_{0.7}\text{Ni}_{0.3}\text{HCF}$ could even recover to the initial value, while the capacity of CoHCF cannot be recovered because of a greater structural change. After 500 cycles, $\text{Co}_{0.7}\text{Ni}_{0.3}\text{HCF}$ shows a higher sodium ions diffusion coefficient (D_{Na^+}) than that of CoHCF confirmed by GITT tests [**Supplementary Figure 5**], which may be attributed to its high ion mobility benefited from Ni substitution. EIS curves of $\text{Co}_{0.7}\text{Ni}_{0.3}\text{HCF}$ and CoHCF before and after cycling are shown in **Supplementary Figure 6**. The Rct of $\text{Co}_{0.7}\text{Ni}_{0.3}\text{HCF}$ before cycling is significantly smaller than that of CoHCF due to the good ionic/electronic conductivity brought by Ni substitution. The Rct of both electrodes increase after 500 cycles, but the Rct of $\text{Co}_{0.7}\text{Ni}_{0.3}\text{HCF}$ is still lower than that of CoHCF , which also explains the better reversibility and rate capability of $\text{Co}_{0.7}\text{Ni}_{0.3}\text{HCF}$.

Figure 3 presents the electrochemical performance of $\text{Co}_{0.7}\text{Ni}_{0.3}\text{HCF}$ and CoHCF from -30 °C to 60 °C. As shown in **Figure 3A** and **B**, CoHCF only delivers 25.7 mAh g^{-1} at the rate of 0.1 C at -30 °C. It is remarkable that $\text{Co}_{0.7}\text{Ni}_{0.3}\text{HCF}$ can be charged at such a low temperature of -30 °C, while most secondary batteries cannot be charged at low temperatures. Moreover, it exhibits a high specific capacity of 109 mAh g^{-1} at 0.1 C

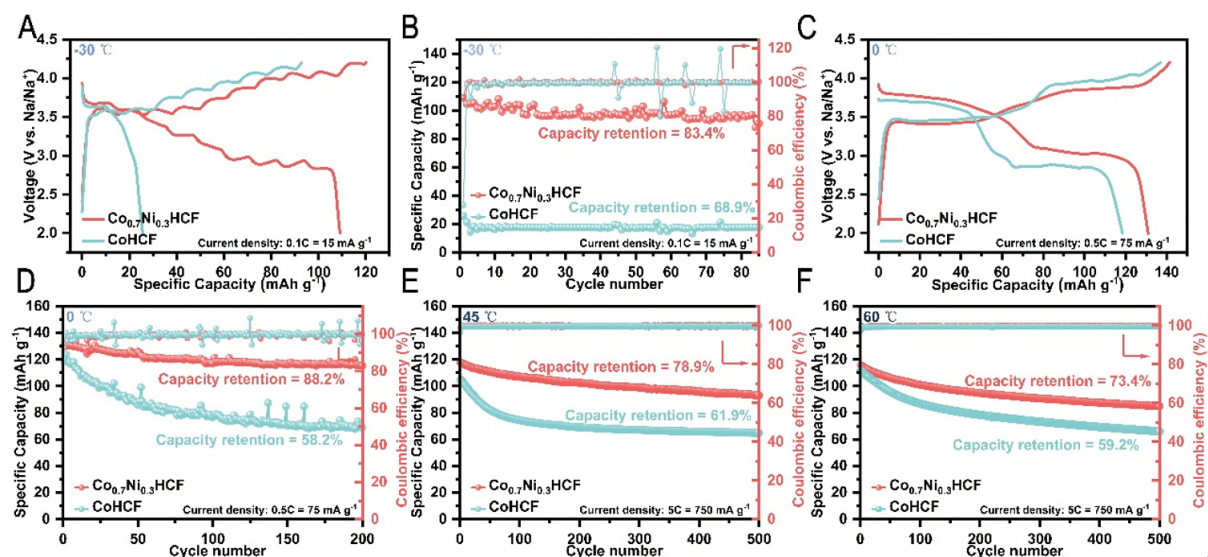


Figure 3. Electrochemical properties of Co_{0.7}Ni_{0.3}HCF and CoHCF at different temperatures (-30/0/45/60 °C). (A and C) Charge/discharge voltage profiles of Co_{0.7}Ni_{0.3}HCF and CoHCF at different rates (0.1/0.5 C) and temperatures (-30/0 °C). (B and D-F) Long-cycle performance of Co_{0.7}Ni_{0.3}HCF and CoHCF at different rates (0.1/0.5/5/5 C) and temperatures (-30/0/45/60 °C) from 2 V to 4.2 V.

and 83.4% capacity retention over 80 cycles at -30 °C. Figure 3C shows the charge/discharge voltage profiles of Co_{0.7}Ni_{0.3}HCF and CoHCF at 0 °C. Compared to CoHCF, Co_{0.7}Ni_{0.3}HCF shows two obvious charge/discharge platforms with much less polarization. At 0.5 C, the Co_{0.7}Ni_{0.3}HCF shows an initial discharge capacity of 130.9 mA h g⁻¹ and maintains the capacity up to 115.5 mAh g⁻¹ after 200 cycles at 0 °C [Figure 3D]. As shown in Figure 3E and F, Co_{0.7}Ni_{0.3}HCF also exhibits great cyclability at high temperatures. It delivers an initial capacity of about 120 mA h g⁻¹ at a high rate of 5 C with capacity retention of 78.9% and 73.4% at 45 °C and 60 °C, respectively. As a comparison, CoHCF only exhibits about 110 mA h g⁻¹ and maintains 61.9% and 59.2% of its capacity at the same temperature and current density, respectively. In summary, Co_{0.7}Ni_{0.3}HCF shows improved electrochemical performance than CoHCF over a wide temperature range. Additionally, we have made a comparison between the outstanding all-temperature electrochemical performance of Co_{0.7}Ni_{0.3}HCF in this work and the existing literature [Supplementary Figure 4B]. Co_{0.7}Ni_{0.3}HCF has a wider range of charging and discharging temperatures and shows higher capacity at various current densities and temperatures, especially at high current density and extremely low temperatures.

Sodium-ion storage mechanism investigation

Figure 4A and B display *ex-situ* XRD patterns of Co_{0.7}Ni_{0.3}HCF and CoHCF at various charge/discharge depth. The crystalline structures of Co_{0.7}Ni_{0.3}HCF and CoHCF electrodes in the initial state are both monoclinic, indicating the Na content in Co_{0.7}Ni_{0.3}HCF and CoHCF frameworks is high. During the charging process from 2 V to 4.2 V, sodium ions are gradually extracted from the lattice, and peaks of 200 plane at around 17° and 400 plane at around 35° shift to a higher angle gradually, showing that the lattice size decreases gradually during a continuous solid-solution reaction mechanism. As the sodium ions further de-intercalated, XRD results show a merging of multi-peak from 23° to 25° indexed as -211, 020, 002 and 211 of monoclinic structure into a single sharp peak of 220 of cubic phase around 25°, indicating a two-phase transition from monoclinic phase to cubic phase. This is consistent with the previous reports^[39] that when Na content is relatively low, the system energy tends to be reduced by correcting the distorted monoclinic framework skeleton, and it is the opposite when Na content is high. The lattice with very low Na

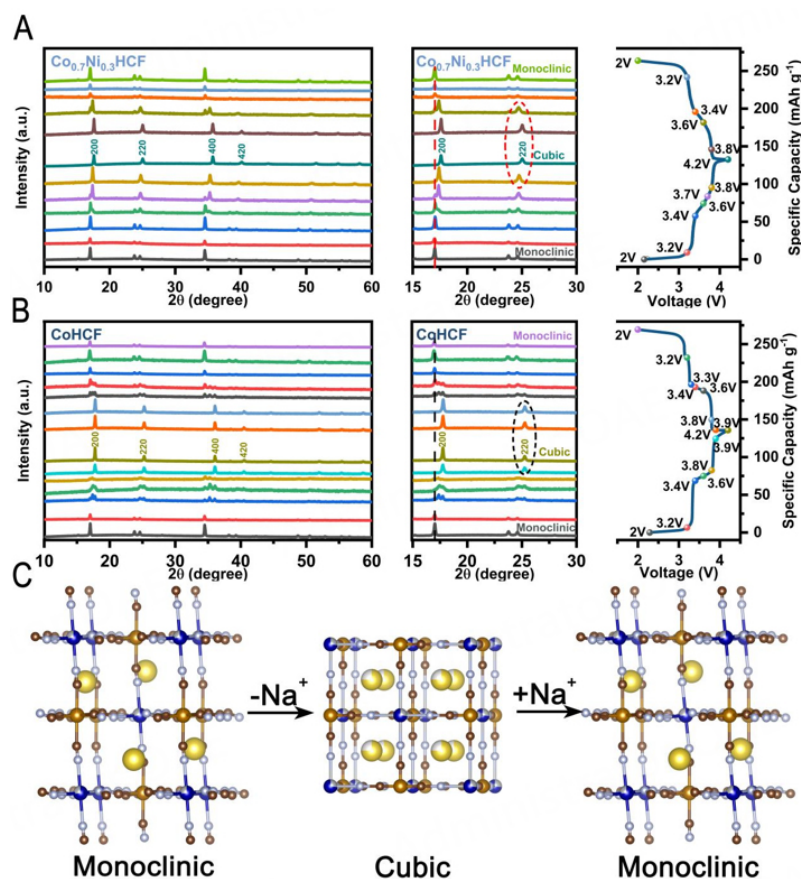


Figure 4. Sodium storage mechanism at 25 °C. *Ex-situ* XRD patterns of the (A) $\text{Co}_{0.7}\text{Ni}_{0.3}\text{HCF}$ and (B) CoHCF electrodes at different states during the first cycle. The dots in different colors in the charge-discharge curves (right) represent the states tested by *ex-situ* XRD. (C) Schematic phase evolution as a result of Na^+ extraction/insertion from/into the $\text{Co}_{0.7}\text{Ni}_{0.3}\text{HCF}$.

content tends to exhibit cubic phase with lower energy rather than monoclinic phase to maintain stability. When charged to 4.2 V, $\text{Co}_{0.7}\text{Ni}_{0.3}\text{HCF}$ and CoHCF have completely transformed into the cubic phase, indicating that large amounts of sodium ions are released, which corresponds to the high charge specific capacity. The Rietveld refinements and schematic illustrations of the cubic phase (Charged) of $\text{Co}_{0.7}\text{Ni}_{0.3}\text{HCF}$ and CoHCF are shown in [Supplementary Figure 7](#), the structural parameters of which are shown in [Supplementary Table 2](#). During the discharging process from 4.2 V to 2 V, as sodium ions insert into the lattice, the energy of the system tends to decrease by twisting the skeleton, so the crystalline structure transitions to a more stable monoclinic phase. During the charging and discharging process, the lattice shows a reversible two-phase transition process from monoclinic to cubic phase, as shown in [Figure 4C](#).

Even though the specific capacity of CoHCF at a low rate is high, the cycle stability is poor for long-term cycling because of incompletely reversible lattice distortion. According to the much smaller peaks shift for $\text{Co}_{0.7}\text{Ni}_{0.3}\text{HCF}$ in the *ex-situ* XRD patterns during the charging and discharging process, the volume change of $\text{Co}_{0.7}\text{Ni}_{0.3}\text{HCF}$ lattice during cycling is significantly lower than that of CoHCF. The volume change rate during the discharge process can be calculated according to the Rietveld refinements of fully charged and discharged electrodes. The volume change rate of $\text{Co}_{0.7}\text{Ni}_{0.3}\text{HCF}$ and CoHCF during the two-phase transition is about 10.78% and 14.27%, respectively. Detailed lattice parameters are provided in [Supplementary Figure 8](#) and [Supplementary Table 3](#). The result indicates that the better cycling stability of $\text{Co}_{0.7}\text{Ni}_{0.3}\text{HCF}$ than CoHCF is due to the suppressed structural distortion and the reversibility of volume

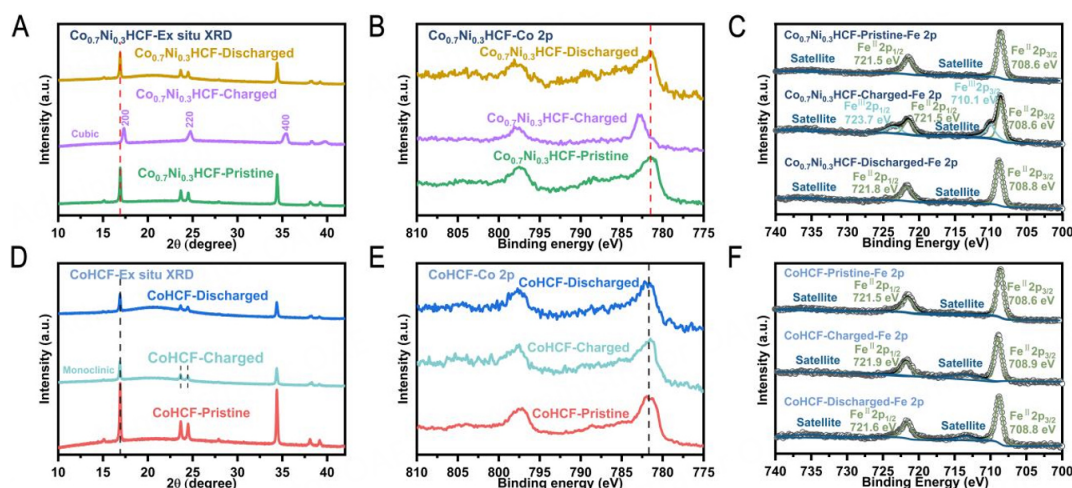


Figure 5. Sodium storage mechanism at $-30\text{ }^{\circ}\text{C}$. (A and D) *Ex-situ* XRD patterns. (B and E) *Ex-situ* XPS Co 2p spectra and (C and F) *Ex-situ* XPS Fe 2p of $\text{Co}_{0.7}\text{Ni}_{0.3}\text{HCF}$ and CoHCF at different redox states including as-prepared electrodes ($\text{Co}_{0.7}\text{Ni}_{0.3}\text{HCF}/\text{CoHCF}$ -Pristine), electrodes charged to 4.2 V ($\text{Co}_{0.7}\text{Ni}_{0.3}\text{HCF}/\text{CoHCF}$ -Charged) and electrodes charged to 4.2 V and then discharged to 2.0 V ($\text{Co}_{0.7}\text{Ni}_{0.3}\text{HCF}/\text{CoHCF}$ -Discharged).

change determines the cycling stability. Since the two-phase transition is caused by sufficient sodium ions de-/insertion, phase transition always relates to high capacity. Therefore, considering both the capacity and cycling stability, it is of particular significance to control the lattice distortion within a small range while ensuring more sodium ions are de-/intercalated. Here, Ni substitution in CoHCF has been successfully achieved.

Furthermore, XRD patterns and FTIR spectra of $\text{Co}_{0.7}\text{Ni}_{0.3}\text{HCF}$ and CoHCF electrodes collected before and after 500 cycles are shown in [Supplementary Figure 9](#). After 500 cycles, the peak corresponding to the 200 plane of CoHCF shifts from 16.897° to 16.940° (0.043° offset), indicating that the Na content of CoHCF electrode is reduced after 500 cycles, while the peak of $\text{Co}_{0.7}\text{Ni}_{0.3}\text{HCF}$ mainly does not shift, suggesting robust structural stability during long-term cycling. The Rietveld refinements of $\text{Co}_{0.7}\text{Ni}_{0.3}\text{HCF}$ and CoHCF after 500 cycles are shown in [Supplementary Figure 10](#). According to the lattice parameters of $\text{Co}_{0.7}\text{Ni}_{0.3}\text{HCF}$ and CoHCF before and after 500 cycles [[Supplementary Table 4](#)], the volume change rates before and after 500 cycles of $\text{Co}_{0.7}\text{Ni}_{0.3}\text{HCF}$ and CoHCF are 0.04 % and 1.12 %, respectively. According to the occupancy of sodium ions in the lattice, reduced percentages of sodium ions of $\text{Co}_{0.7}\text{Ni}_{0.3}\text{HCF}$ and CoHCF before and after 500 cycles are 0.79% and 4.01%, respectively. Therefore, it can be preliminarily judged that $\text{Co}_{0.7}\text{Ni}_{0.3}\text{HCF}$ has a more stable structure.

It is also confirmed by the results of FTIR tests at different cycles. The absorption peaks at $\sim 2075\text{ cm}^{-1}$ corresponding to the stretching vibration of $\text{C}\equiv\text{N}$ of $\text{Co}_{0.7}\text{Ni}_{0.3}\text{HCF}$ and CoHCF shift to higher wavenumbers (4 cm^{-1} and 9 cm^{-1} offset, respectively) after 500 cycles, indicating that the average valence state of transition metals in CoHCF is higher than that in $\text{Co}_{0.7}\text{Ni}_{0.3}\text{HCF}$ ^[48,49]. This result indicates that the percentage of sodium retained in $\text{Co}_{0.7}\text{Ni}_{0.3}\text{HCF}$ after long-term cycling is higher than that in CoHCF compared with pristine electrodes.

As shown in [Figure 5A](#), the multi-peak from 23° to 25° indexed as -211 , 020 , 002 and 211 of monoclinic structure transform into a single peak corresponding to the 220 plane of cubic phase around 25° , indicating the phase transition from monoclinic to cubic has occurred at $-30\text{ }^{\circ}\text{C}$ in charged $\text{Co}_{0.7}\text{Ni}_{0.3}\text{HCF}$, which is owing to the extraction of enough sodium ions from the lattice. While discharge from 4.2 to 2 V at $-30\text{ }^{\circ}\text{C}$,

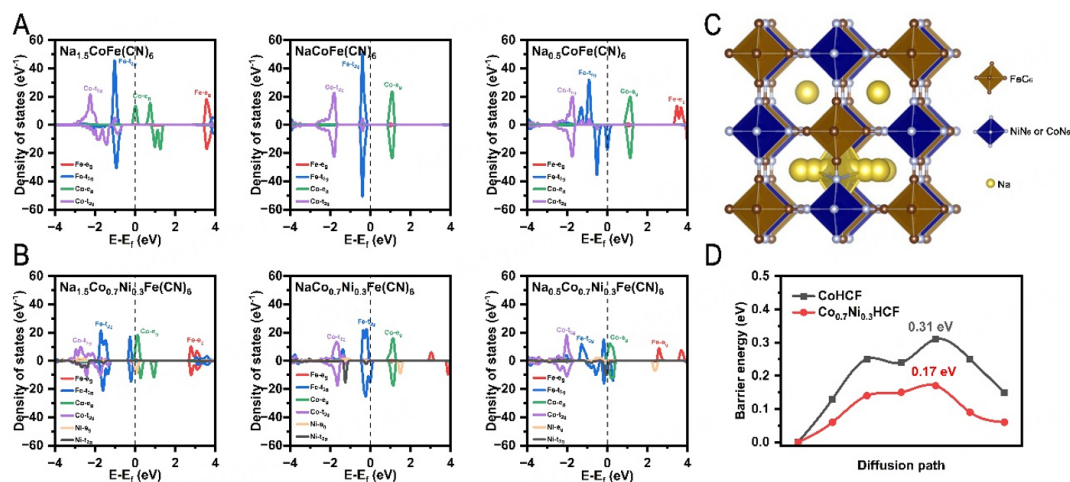


Figure 6. First-principles calculations. Electronic density of states of (A) CoHCF and (B) Co_{0.7}Ni_{0.3}HCF at different Na concentrations, including Na-1.5, Na-1, and Na-0.5. (C) The schematic of the calculated Na⁺ migration paths within the lattice of the Co_{0.7}Ni_{0.3}HCF and CoHCF model structures. (D) Migration energy barriers of the Na⁺-ion diffusion within the lattice of the Co_{0.7}Ni_{0.3}HCF and CoHCF.

the phase transition occurs reversibly from cubic to monoclinic phase, indicating the extracted sodium ions can reversibly insert into the lattice even at -30 °C. This reversible two-phase transition is similar to that occurring at room temperature of Co_{0.7}Ni_{0.3}HCF, demonstrating a fast ion transfer kinetics in Co_{0.7}Ni_{0.3}HCF. In contrast, Figure 5D presents no phase transition for charged CoHCF, which maintains the monoclinic phase during the charging and discharging process at -30 °C, suggesting that too few sodium ions are extracted from the framework of CoHCF to induce a phase transition. This result can be ascribed to the fact that sodium ions in CoHCF are difficult to migrate at -30 °C and most sodium ions are still preserved in the lattice. The XPS^[50] test results of Co 2p at -30 °C in Figure 5B and E show that the binding energy of Co 2p peak in CoHCF almost does not change during cycling at -30 °C, while the peak of Co 2p exhibits a significant peak shift towards higher bind energy from Co_{0.7}Ni_{0.3}HCF-Pristine to Co_{0.7}Ni_{0.3}HCF-Charged, revealing obvious electronic migration has occurred in the cobalt atoms of Co_{0.7}Ni_{0.3}HCF-Charged. The XPS data of Fe 2p at -30 °C are shown in Figure 5C and F for Co_{0.7}Ni_{0.3}HCF and CoHCF samples. Co_{0.7}Ni_{0.3}HCF-Charged can be fitted with an obvious Fe^{III} 2p peak located at 710.1 eV and 723.7 eV, which is not found in CoHCF-Charged. It is clear that the electrochemical activity of transition metals in CoHCF is severely inhibited. The valence change of transition metals shows that Co_{0.7}Ni_{0.3}HCF has higher redox activity at low temperatures.

According to the partial density of states (PDOS) of Co_{0.7}Ni_{0.3}HCF and CoHCF, the bandgap of Co_{0.7}Ni_{0.3}HCF is obviously reduced after the replacing of Co by Ni, leading to the enhanced electronic conductivity, which is beneficial for redox kinetics. Figure 6A shows the PDOS of CoHCF with different sodium content during sodium extraction process. The Co e_g orbital of Na_{1.5}CoFe(CN)₆ is close to the Fermi level, which means Co²⁺ is redox active. With the extraction of sodium ions, the t_{2g} orbital of Fe gradually approaches the Fermi level, indicating that Fe participates in the redox reaction when further charging. The above analysis of electronic density of states reveals the charge-transfer mechanism of CoHCF, which matches well with the CV measurements. While in Co_{0.7}Ni_{0.3}HCF, both Co e_g and Fe t_{2g} orbitals locate at Fermi level in the Na-rich and Na-poor samples, as shown in Figure 6B. It can be seen that the charge-transfer mechanism of each transition metal ion in Co_{0.7}Ni_{0.3}HCF may be different from CoHCF, although the CV curves of CoHCF and Co_{0.7}Ni_{0.3}HCF are two similar peaks^[51]. In addition, it can be found that Ni has involved in charge transfer along frameworks throughout the full redox reaction; the electrons around Ni have delocalized due to the variation of coordination environment, which is also of great benefit to obtain

the enhanced conductivity in $\text{Co}_{0.7}\text{Ni}_{0.3}\text{HCF}$ ^[39]. Furthermore, the calculated results based on density functional theory (DFT) [Figure 6C and D] prove that the energy migration barriers of Na^+ -ions in $\text{Co}_{0.7}\text{Ni}_{0.3}\text{HCF}$ are lower than that in CoHCF, which is consistent with GITT experiment results. Schematic illustrations of the structures of $\text{Co}_{0.7}\text{Ni}_{0.3}\text{HCF}$ and CoHCF unit cell of calculation model are shown in Supplementary Figure 11. All of these calculations demonstrate that the electronic conductivity, redox activity and ion mobility of $\text{Co}_{0.7}\text{Ni}_{0.3}\text{HCF}$ are enhanced effectively than those of un-substituted sample (CoHCF), which provides enlightenment that a small amount of Ni in the lattice of PBAs can promote the electron transfer and ion diffusion, as well as stabilize the frameworks.

CONCLUSIONS

In conclusion, to address the low actual specific capacity, poor cycling and poor rate capability of CoHCF as the cathode material of SIBs, partial substitution of Co by Ni is proposed in low-defect and Na-enriched CoHCF sample. The introduction of Ni inhibits large lattice distortion during cycling, improves the electronic conductivity and reduces the migration barrier of sodium ions. Benefiting from the structural effect of Ni substitution, $\text{Co}_{0.7}\text{Ni}_{0.3}\text{HCF}$ not only exhibits high capacity up to 142.2 mAh g^{-1} , but also achieves high capacity retention of more than 80% after 500 cycles at room temperature. Even at such a low temperature of $-30 \text{ }^\circ\text{C}$, a reversible two-phase transition between monoclinic phase and cubic phase is occurred due to adequate sodium-ions insertion and extraction, which provides a high specific capacity of 109 mAh g^{-1} . Moreover, $\text{Co}_{0.7}\text{Ni}_{0.3}\text{HCF}$ also shows stable electrochemical performance at high temperatures of $45 \text{ }^\circ\text{C}$ and $60 \text{ }^\circ\text{C}$ owing to suppressed lattice variation and stable framework. It demonstrates that Ni-substituted double redox active PBAs are potential candidates for cathode material in all-climate sodium-ion batteries due to their unique structural characteristics. However, Co and Ni are too expensive to apply on a large scale, so the exploration of the next generation of low-cost all-climate sodium-ion batteries is worth studying.

DECLARATIONS

Authors' contributions

Methodology, formal analysis and writing manuscript: Zhang J, Wan J

Data analysis and technical support: Ou M, Liu S, Huang B

Data acquisition: Xu J, Lin Y

Supervision, writing - review and editing: Sun S, Xu Y, Fang C, Han J

Availability of data and materials

The data supporting our findings can be found in the [Supplementary Material](#).

Financial support and sponsorship

This work was supported by National Natural Science Foundation of China (Grant No. 52172201, 51732005, 51902118, 52102249), China Postdoctoral Science Foundation (Grant Nos. 2019M662609 and 2020T130217), and the international postdoctoral exchange fellowship program No. PC2021026 for financial support. We thank the Analytical and Testing Centre and the State Key Laboratory of Materials Processing and Die & Mould Technology and the Experiment Center for Advanced Manufacturing and Technology in School of Mechanical Science & Engineering of HUST for the material characterization.

Conflicts of interest

All authors declared that there are no conflicts of interest.

Ethical approval and consent to participate

Not applicable.

Consent for publication

Not applicable.

Copyright

© The Author(s) 2023.

REFERENCES

1. Evarts EC. Lithium batteries: to the limits of lithium. *Nature* 2015;526:S93-5. [DOI](#)
2. Larcher D, Tarascon JM. Towards greener and more sustainable batteries for electrical energy storage. *Nat Chem* 2015;7:19-29. [DOI](#)
3. Qian J, Wu C, Cao Y, et al. Prussian blue cathode materials for sodium-ion batteries and other ion batteries. *Adv Energy Mater* 2018;8:1702619. [DOI](#)
4. Fang Y, Luan D, Lou XW. Recent advances on mixed metal sulfides for advanced sodium-ion batteries. *Adv Mater* 2020;32:e2002976. [DOI](#)
5. Li Y, Yang Y, Lu Y, et al. Ultralow-concentration electrolyte for na-ion batteries. *ACS Energy Lett* 2020;5:1156-8. [DOI](#)
6. Piernas Muñoz MJ, Castillo Martínez E. Electrochemical performance of prussian blue and analogues in aqueous rechargeable batteries. In *Prussian Blue Based Batteries*; 2018, pp. 23-44. [DOI](#)
7. Wessells CD, Peddada SV, Huggins RA, et al. Nickel hexacyanoferrate nanoparticle electrodes for aqueous sodium and potassium ion batteries. *Nano Lett* 2011;11:5421-5. [DOI](#)
8. Peng J, Gao Y, Zhang H, et al. Ball milling solid-state synthesis of highly crystalline prussian blue analogue $\text{Na}_2\text{-xMnFe}(\text{CN})_6$ cathodes for all-climate sodium-ion batteries. *Angew Chem Int Ed* 2022;61:e202205867. [DOI](#)
9. Imanishi N, Morikawa T, Kondo J, et al. Lithium intercalation behavior into iron cyanide complex as positive electrode of lithium secondary battery. *J Power Sources* 1999;79:215-9. [DOI](#)
10. Pramudita JC, Schmid S, Godfrey T, et al. Sodium uptake in cell construction and subsequent in operando electrode behaviour of Prussian blue analogues, $\text{Fe}[\text{Fe}(\text{CN})_6]_{(1-x)}\cdot y\text{H}_2\text{O}$ and $\text{FeCo}(\text{CN})_6$. *Phys Chem Chem Phys* 2014;16:24178-87. [DOI](#)
11. Peng J, Zhang W, Liu Q, et al. Prussian blue analogues for sodium-ion batteries: past, present, and future. *Adv Mater* 2022;34:2108384. [DOI](#)
12. Wu X, Wu C, Wei C, et al. Highly crystallized $\text{Na}_2\text{CoFe}(\text{CN})_6$ with suppressed lattice defects as superior cathode material for sodium-ion batteries. *ACS Appl Mater Interfaces* 2016;8:5393-9. [DOI](#)
13. Shang Y, Li X, Song J, et al. Unconventional Mn vacancies in Mn-Fe prussian blue analogs: suppressing jahn-teller distortion for ultrastable sodium storage. *Chem* 2020;6:1804-18. [DOI](#)
14. Jiang M, Hou Z, Wang J, et al. Balanced coordination enables low-defect Prussian blue for superfast and ultrastable sodium energy storage. *Nano Energy* 2022;102:107708. [DOI](#)
15. Peng J, Wang J, Yi H, et al. A Dual-insertion type sodium-ion full cell based on high-quality ternary-metal prussian blue analogs. *Adv Energy Mater* 2018;8:1702856. [DOI](#)
16. Wang W, Gang Y, Hu Z, et al. Reversible structural evolution of sodium-rich rhombohedral Prussian blue for sodium-ion batteries. *Nat Commun* 2020;11:980. [DOI](#)
17. Gong W, Wan M, Zeng R, et al. Ultrafine prussian blue as a high-rate and long-life sodium-ion battery cathode. *Energy Technol* 2019;7:1900108. [DOI](#)
18. Han B, Zhang D, Liu X, et al. Ordered assembly of potassium cobalt hexacyanoferrate hollow multivoid nanocuboid arrays for high-performance aqueous K-ion batteries towards all-climate energy storage. *J Mater Chem A* 2022;10:13508-18. [DOI](#)
19. Tang Y, Li W, Feng P, et al. Investigation of alkali-ion (Li, Na and K) intercalation in manganese hexacyanoferrate $\text{K}_x\text{MnFe}(\text{CN})_6$ as cathode material. *Chem Eng J* 2020;396:125269. [DOI](#)
20. Shao T, Li C, Liu C, et al. Electrolyte regulation enhances the stability of Prussian blue analogues in aqueous Na-ion storage. *J Mater Chem A* 2019;7:1749-55. [DOI](#)
21. Feng F, Chen S, Zhao S, et al. Enhanced electrochemical performance of MnFe@NiFe Prussian blue analogue benefited from the inhibition of Mn ions dissolution for sodium-ion batteries. *Chem Eng J* 2021;411:128518. [DOI](#)
22. Gebert F, Cortie DL, Bouwer JC, et al. Epitaxial nickel ferrocyanide stabilizes jahn-teller distortions of manganese ferrocyanide for sodium-ion batteries. *Angew Chem Int Ed* 2021;60:18519-26. [DOI](#)
23. Qiao Y, Wei G, Cui J, et al. Prussian blue coupling with zinc oxide as a protective layer: an efficient cathode for high-rate sodium-ion batteries. *Chem Commun* 2019;55:549-52. [DOI](#)
24. Kim J, Yi SH, Li L, et al. Enhanced stability and rate performance of zinc-doped cobalt hexacyanoferrate (CoZnHCF) by the limited crystal growth and reduced distortion. *J Energy Chem* 2022;69:649-58. [DOI](#)
25. Wang B, Han Y, Chen Y, et al. Gradient substitution: an intrinsic strategy towards high performance sodium storage in Prussian blue-based cathodes. *J Mater Chem A* 2018;6:8947-54. [DOI](#)

26. Peng J, Zhang B, Hua W, et al. A disordered Rubik's cube-inspired framework for sodium-ion batteries with ultralong cycle lifespan. *Angew Chem Int Ed* 2023;62:e202215865. DOI
27. Hu J, Tao H, Chen M, et al. Interstitial water improves structural stability of iron hexacyanoferrate for high-performance sodium-ion batteries. *ACS Appl Mater Interfaces* 2022;14:12234-42. DOI
28. Wang W, Gang Y, Peng J, et al. Effect of eliminating water in prussian blue cathode for sodium-ion batteries. *Adv Funct Mater* 2022;32:2111727. DOI
29. Bhatt P, Thakur N, Mukadam MD, et al. Evidence for the existence of oxygen clustering and understanding of structural disorder in prussian blue analogues molecular magnet $M_{1.5}[Cr(CN)_6] \cdot zH_2O$ ($M = Fe$ and Co): reverse monte carlo simulation and neutron diffraction study. *J Phys Chem C* 2013;117:2676-87. DOI
30. Wardecki D, Ojwang DO, Grins J, et al. Neutron diffraction and EXAFS studies of $K_{2x/3}Cu[Fe(CN)_6]_{2/3} \cdot nH_2O$. *Cryst Growth Des* 2017;17:1285-92. DOI
31. Oumellal Y, Delpuech N, Mazouzi D, et al. The failure mechanism of nano-sized Si-based negative electrodes for lithium ion batteries. *J Mater Chem* 2011;21:6201-8. DOI
32. Liu W, Yang M, Wu H, et al. Enhanced cycle life of Si anode for Li-ion batteries by using modified elastomeric binder. *Electrochem Solid-State Lett* 2005;8:A100-3. DOI
33. Kresse G, Hafner J. Ab initio molecular dynamics for liquid metals. *Phys Rev B* 1993;47:558-61. DOI
34. Kresse G, Joubert D. From ultrasoft pseudopotentials to the projector augmented-wave method. *Phys Rev B* 1999;59:1758-75. DOI
35. Perdew JP, Burke K, Ernzerhof M. Generalized gradient approximation made simple. *Phys Rev Lett* 1996;77:3865-68. DOI
36. Chadi DJ. Special points for Brillouin-zone integrations. *Phys Rev B* 1977;16:1746-47. DOI
37. Jain A, Hautier G, Ong SP, et al. Formation enthalpies by mixing GGA and GGA + U calculations. *Phys Rev B* 2011;84:045115. DOI
38. Smidstrup S, Pedersen A, Stokbro K, et al. Improved initial guess for minimum energy path calculations. *J Chem Phys* 2014;140:214106. DOI
39. Xu Y, Wan J, Huang L, et al. Structure distortion induced monoclinic nickel hexacyanoferrate as high-performance cathode for na-ion batteries. *Adv Energy Mater* 2019;9:1803158. DOI
40. Rietveld HM. Line profiles of neutron powder-diffraction peaks for structure refinement. *Acta Cryst* 1967;22:151-2. DOI
41. Loopstra BO, Rietveld HM. Further refinement of the structure of WO. *Acta Cryst* 1969;B25:1420-1. DOI
42. Feng Z, Hou Q, Zheng Y, et al. Method of artificial intelligence algorithm to improve the automation level of Rietveld refinement. *Comp Mater Sci* 2019;156:310-4. DOI
43. Cui X, Feng Z, Jin Y, et al. AutoFP: a GUI for highly automated Rietveld refinement using an expert system algorithm based on FullProf. *J Appl Cryst* 2015;48:1581-6. DOI
44. McCusker LB, Von Dreele RB, Cox DE, et al. Rietveld refinement guidelines. *J Appl Cryst* 1999;32:36-50. DOI
45. Toby BH. R factors in Rietveld analysis: how good is good enough? *Powder Diffr* 2006;21:67-70. DOI
46. Peng J, Ou M, Yi H, et al. Defect-free-induced Na^+ disordering in electrode materials. *Energy Environ Sci* 2021;14:3130-40. DOI
47. Takachi M, Matsuda T, Moritomo Y. Cobalt hexacyanoferrate as cathode material for Na^+ secondary battery. *Appl Phys Express* 2013;6:025802. DOI
48. Li W, Zhang F, Xiang X, et al. Electrochemical properties and redox mechanism of $Na_2Ni_{0.4}Co_{0.6}[Fe(CN)_6]$ Nanocrystallites as high-capacity cathode for aqueous sodium-ion batteries. *J Phys Chem C* 2017;121:27805-12. DOI
49. Luo D, Lei P, Tian G, et al. Insight into electrochemical properties and reaction mechanism of a cobalt-rich prussian blue analogue cathode in a $NaSO_3CF_3$ electrolyte for aqueous sodium-ion batteries. *J Phys Chem C* 2020;124:5958-65. DOI
50. Fang D, He F, Xie J, et al. Calibration of binding energy positions with C1s for XPS results. *J Wuhan Univ Technol-Mat Sci Ed* 2020;35:711-8. DOI
51. Quan J, Xu E, Zhu H, et al. A Ni-doping-induced phase transition and electron evolution in cobalt hexacyanoferrate as a stable cathode for sodium-ion batteries. *Phys Chem Chem Phys* 2021;23:2491-99. DOI